Light-Emitting Diodes

Deutsche Ausgabe: DOI: 10.1002/ange.201905787
Internationale Ausgabe: DOI: 10.1002/anie.201905787

Site-Selective Occupancy of Eu^{2+} Toward Blue-Light-Excited Red Emission in a $Rb_3YSi_2O_7$:Eu Phosphor

Jianwei Qiao, Lixin Ning, Maxim S. Molokeev, Yu-Chun Chuang, Qinyuan Zhang, Kenneth R. Poeppelmeier* und Zhiguo Xia**

Abstract: *Establishing an effective design principle in solid-state materials for a blue-light-excited Eu^{2+}-doped red-emitting oxide-based phosphors remains one of the significant challenges for white light-emitting diodes (WLEDs). Selective occupation of Eu^{2+} in inorganic polyhedra with small coordination numbers results in broad-band red emission as a result of enhanced crystal-field splitting of 5d levels. $Rb_3YSi_2O_7$:Eu exhibits a broad emission band at $\lambda_{max} = 622$ nm under 450 nm excitation, and structural analysis and DFT calculations support the concept that Eu^{2+} ions preferably occupy RbO_6 and YO_6 polyhedra and show the characteristic red emission band of Eu^{2+}. The excellent thermal quenching resistance, high color-rendering index R_a (93), and low CCT (4013 K) of the WLEDs clearly demonstrate that site engineering of rare-earth phosphors is an effective strategy to target tailored optical performance.*

Introduction

Phosphor-converted white-light-emitting diodes (pc-WLEDs) have brought about a new revolution in lighting.[1] Presently, the combination of the blue chip (440–470 nm) and $Y_3Al_5O_{12}:Ce^{3+}$ (YAG:Ce) yellow phosphor is still the common manufacturing method for pc-WLEDs.[1] However, the insufficient emission in the red spectral region (600–700 nm) of YAG:Ce leads to a high correlated color temperature (CCT > 4500 K) and a low color rendering index (CRI < 75) for WLEDs.[2] Realizing illumination-grade lighting requires WLEDs with a high color rendering index (CRI > 90) and low correlated color temperatures (2700–4000 K),[3] and, as such, extensive research has been conducted on different compounds to exploit new red-emitting phosphors. For example, the red-emitting $CaS:Eu^{2+}$ phosphor can achieve a high color rendering index for pc-WLEDs, but the poor thermal and chemical stabilities restrict its applications.[4] Thereafter, Eu^{2+} doped nitride-based red phosphors, including (Ca,Sr)$AlSiN_3:Eu^{2+}$ and $(Ba,Ca)_2Si_5N_8:Eu^{2+}$, have attracted significant attention, which show broad-band red emission in 590–660 nm depending on the chemical compositions, and $Sr[LiAl_3N_4]:Eu^{2+}$ has been reported as the next-generation narrow-band red phosphor for WLEDs.[3,5] However, these nitride phosphors are normally prepared in oxygen/water free glovebox conditions and then fired at high pressure (ca. 1 MPa) and temperature (> 2000 K). Recently, Mn^{4+} doped fluoride phosphors have been extensively studied for pc-WLEDs to improve the color rending owing to its sharp red-emitting lines.[6] Nevertheless, the chemically instability and toxicity of HF used during the synthesis should be carefully considered.[7] Compared with sulfides, nitrides, and fluoride phosphors, oxide-based phosphors including silicates, aluminates, borates, and phosphates, have the advantages of low cost and being environmentally friendly, as well as having versatile crystal and local structures. Surprisingly, there are few reports concerning Eu^{2+} doped oxide-based red phosphors that can be excited by blue light.[8] Therefore, discovery of new oxide-based red-emitting phosphors excited by blue light with good performance is urgent and also requires the

[*] J. W. Qiao, Prof. Dr. Z. G. Xia
School of Materials Sciences and Engineering
University of Science and Technology Beijing
Beijing 100083 (P. R. China)
E-Mail: xiazg@ustb.edu.cn
Prof. Dr. L. X. Ning
Anhui Key Laboratory of Optoelectric Materials Science and Technology, Key Laboratory of Functional Molecular Solids
Ministry of Education, Anhui Normal University
Wuhu 241000 (China)
E-Mail: ninglx@mail.ahnu.edu.cn
Prof. Dr. M. S. Molokeev
Laboratory of Crystal Physics, Kirensky Institute of Physics
Federal Research Center KSC SB RAS
Krasnoyarsk 660036 (Russia)
and
Siberian Federal University
Krasnoyarsk 660041 (Russia)
and
Department of Physics, Far Eastern State Transport University
Khabarovsk, 680021 (Russia)
Y. C. Chuang
National Synchrotron Radiation Research Center
Hsinchu 300 (Taiwan)
Prof. Dr. Q. Y. Zhang, Prof. Dr. Z. G. Xia
State Key Laboratory of Luminescent Materials and Devices and Institute of Optical Communication Materials
South China University of Technology
Guangzhou, 510641 (China)
E-Mail: xiazg@scut.edu.cn
Prof. Dr. K. R. Poeppelmeier
Department of Chemistry, Northwestern University
2145 Sheridan Road, Evanston, IL 60208-3113 (USA)
E-Mail: krp@northwestern.edu

Supporting information and the ORCID identification number(s) for the author(s) of this article can be found under: https://doi.org/10.1002/anie.201905787.

establishment of an effective design principle during materials exploration.

Normally, the energy gap between the 4f ground state and the 5d excited state for free Eu^{2+} ions is about 4.2 eV (34000 cm^{-1}).[9] When the Eu^{2+} ions are doped into a given host lattice, the 5d excited state will interact with the coordinating environment, leading to spectroscopic red-shift as a result of crystal field splitting and centroid shift.[10] For nitride-based red phosphors, such as $CaAlSiN_3$:Eu, $Sr_2Si_5N_8$:Eu, and $Sr[LiAl_3N_4]$:Eu, Eu^{2+} ions are surrounded by a network of condensed MN_4 tetrahedra (M = Si, Al, Li) and the coordination numbers for the activators are 5, 8, and 8, respectively.[3,5a,b] The polarizable nitridic surroundings lower the 5d excited state of Eu^{2+} owing to the strong nephelauxetic effect, and thus result in red emission. For CaS:Eu^{2+}, one Ca and six S atoms form a symmetric octahedron,[4] and the occupation of Eu^{2+} ions in polyhedra CaO_6 with small coordination numbers results in a large crystal field splitting and contributes to red emission. Accordingly, an effective strategy to reduce transition energy from 5d to 4f levels is to increase the centroid shift of 5d levels. However, it is difficult to achieve this goal in oxide phosphors owing to the weak covalent interaction between the Eu^{2+} and O^{2-} compared with that of Eu^{2+} and N^{3-}.[11] The other way to achieve red emission in Eu^{2+}-doped oxide phosphor is to find new oxide hosts with strong crystal field strength.[12] Typically, transition-metal and main-group elements have coordination numbers (CNs) = 2–6, while rare-earth ions have CNs ≥ 6. The design principle on the discovery of Eu^{2+}-doped oxide-based red-emitting phosphors has been applied to the screening of the site occupation of the activators located in the polyhedra with small CNs. The novel oxide-based $Rb_3YSi_2O_7$ host possesses three different polyhedra, YO_6, $Rb1O_9$, and $Rb2O_6$. Importantly, Eu^{2+} ions selectively occupy the YO_6 and $Rb2O_6$ polyhedra with small CNs that brought about a large crystal field splitting of 5d levels. Therefore, the as-prepared $Rb_3YSi_2O_7$:Eu phosphor shows a broad-band emission from 550 to 750 nm in the red spectral region, and the fraction of near infrared emission is very small compared to the dominant red emission. Photoluminescence properties and Eu^{2+}/Eu^{3+} site occupation mechanism in single-phased $Rb_3YSi_2O_7$:Eu were studied in detail by Rietveld refinement and density functional theory (DFT) calculations, respectively. Our research will initiate and guide more exploration on discovering new red-emitting oxide phosphors.

Results and Discussion

Crystal and Local Structure Analysis

To characterize the phase purity and structure of $Rb_3YSi_2O_7$:0.02Eu powder, Rietveld refinement was conducted with the high-quality synchrotron XRD data by using TOPAS 4.2,[13] as shown in Figure 1a. Almost all peaks, except for tiny peaks of Y_2O_3 impurity (weight ca. 0.26%), were indexed by hexagonal cell ($P6_3/mmc$) with parameters close to $K_3YSi_2O_7$.[14] Therefore, $K_3YSi_2O_7$ structure was taken as

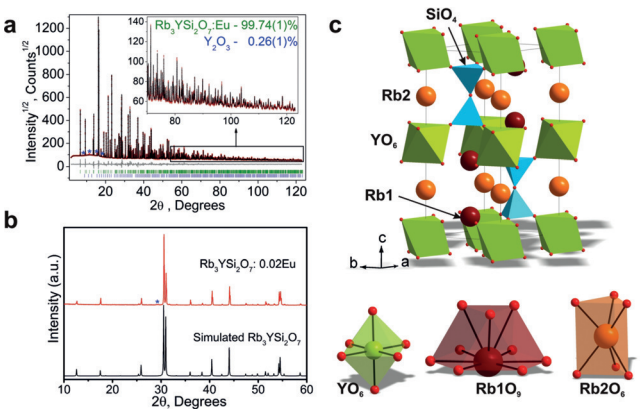

Figure 1. a) Rietveld refinement of the synchrotron XRD profile of $Rb_3YSi_2O_7$:0.02Eu phosphor to determine the crystal structure of $Rb_3YSi_2O_7$. b) Comparison of the powder XRD pattern and the calculated profile from synchrotron XRD. c) Crystal structure of $Rb_3YSi_2O_7$ and the coordination of the [YO_6], [$Rb1O_9$] and [$Rb2O_6$] polyhedra.

the starting model for Rietveld refinement with K^+ sites occupied by Rb^+ ions. A comparison of the measured and calculated XRD patterns is shown in Figure 1b, also suggesting the successful preparation and phase purity. The refinement for $Rb_3YSi_2O_7$:0.02Eu gave low *R*-factors, and the derived unit cell parameters are listed in the Supporting Information, Table S1. The crystallographic information file (CIF) of this new phase $Rb_3YSi_2O_7$ is presented in the Supporting Information.[25] Coordinates of atoms in the unit cell and the main bond lengths are listed in Table S2 and Table S3, respectively. The unit-cell crystal structure of $Rb_3YSi_2O_7$ is given in Figure 1c with the sites of Rb1, Rb2, and [YO_6] indicated, and two silicon tetrahedra form bent Si_2O_7 pyrosilicate units with bridging Si-O-Si linkages of 108.58°. Moreover, the [YO_6], [$Rb1O_9$] and [$Rb2O_6$] polyhedra are also given in Figure 1c.

The initial model for the refinement to determine the Eu doping site was applied in all the three cation (Y^{3+}, $Rb1^+$, and $Rb2^+$) sites, but the result showed nonzero Eu occupancy only at the Y^{3+} site (Supporting Information, Table S2). It should be pointed out, however, that this does not exclude the existence of tiny quantity of Eu occupying the Rb^+ site that cannot be easily detected. The estimated standard deviation (esd) for refinement of Eu occupancy at each site is about 0.0008 (0.08%), which means that the Rietveld refinement cannot determine Eu occupancy less than 3 esd = 0.24%.[15] Indeed, Eu^{2+} ions are present at Rb^+ sites, giving red luminescence even stronger than that from Eu^{3+}, as will be shown later. On the basis of comparison between the ionic radii of Eu^{2+}, Eu^{3+}, Rb^+, and Y^{3+} in the same fold of coordination (Supporting Information, Table S4), it is expected that the Eu ions located at Y^{3+} sites are mostly Eu^{3+}, while those, if any, at Rb^+ sites are Eu^{2+}.[16] Minor Eu^{2+} doping at Rb^+ site can be charge-compensated by the Rb vacancy or Eu^{2+} doping at Y^{3+} site, as discussed below, and the intrinsic charge balance will be more stable compared to the extrinsic one realized by introducing impurities (or codoping). Eu-*L*3 edge X-ray absorption near-edge structure (XANES) spectra of $Rb_3YSi_2O_7$:0.02Eu and Eu_2O_3, respectively, are shown in

the Supporting Information, Figure S1. $Rb_3YSi_2O_7$:0.02Eu demonstrates a strong peak at 6982 eV, similar with the peak of Eu_2O_3, being ascribed to the $2p_{3/2}\rightarrow 5d$ transition of Eu^{3+}. Moreover, the long tail on the low-energy side signifies the presence of a small amount of Eu^{2+} in $Rb_3YSi_2O_7$:0.02Eu.[17] Thus, most Eu ions are presented as Eu^{3+} in $Rb_3YSi_2O_7$ with a tiny amount of Eu^{2+}, in line with Rietveld refinement results discussed above. The SEM and elemental mapping images of $Rb_3YSi_2O_7$, respectively, are shown in the Supporting Information, Figure S2a,b. Clearly, the morphology of microcrystals is similar with a size range around 50 μm, and the rough surface will limit luminous efficiency to some extent. The elemental mapping images (Supporting Information, Figure S2b) certify that Rb, Y, Si, O elements are homogeneously distributed in the phosphor particles. Moreover, the atomic percentage of Rb, Y, Si is about 38.75:13.16:22.28, which is very close to the theoretical percentage of 3:1:2 (Supporting Information, Figure S2c).

Photoluminescence Properties

Normally, it is hard to achieve red emission of Eu^{2+} in oxide phosphors, especially upon the excitation of blue light, owing to the weak covalent interaction between the Eu^{2+} and O^{2-}. Thus, the special local structure and Eu^{2+} occupancy as discussed above can account for the as-observed red emission. Accordingly, Figure 2a displays the excitation and emission spectra of $Rb_3YSi_2O_7$:0.02Eu measured at room temperature. The inset shows that the sample exhibits a uniform light red tint under natural daylight, and a bright red-light emission under NUV light (365 nm) excitation. Under 450 nm blue-light excitation, the PL spectrum consists a broad band (red curve) ranging from 575 to 800 nm and peaking at 622 nm with a full width at half maximum (FWHM) of 124 nm. This emission band is obviously attributed to 5d→4f transition of Eu^{2+} ions. When monitoring the 622 nm emission, the excitation band (black curve) extends from 300 to 550 nm covering NUV-blue spectral region with maximum at around 450 nm. Sharp lines are superimposed upon the 4f→5d band spectrum on the long-wavelength side and can be attributed to intra-configurational 4f→4f absorption of Eu^{3+}. This is understandable since the monitored emission at 622 nm also contains contribution from $(4f^6)^5D_0\rightarrow(4f^6)^7F_2$ transitions of Eu^{3+}. To demonstrate this, the emission spectrum under 254 nm excitation corresponding to $O^{2-}\rightarrow Eu^{3+}$ charge transfer (CT) transition was measured and also displayed in Figure 2a (green curve). The typical emission pattern of Eu^{3+} was observed corresponding to $^5D_0\rightarrow{}^7F_J$ transitions within the $4f^6$ configuration, with the highest-intensity emission being at 592 nm corresponding to $^5D_0\rightarrow{}^7F_1$ transition. Moreover, the excitation spectrum (blue curve) of the 592 nm emission exhibits a spectral profile similar to that of the 622 nm emission except for the more obvious presence of the CT band at 254 nm. Furthermore, comparison of the emission spectra for Eu^{3+} and Eu^{2+} shows that, although most Eu ions in $Rb_3YSi_2O_7$ exist in the form of Eu^{3+} located at Y^{3+} sites, relatively very low level of Eu^{2+} are indeed present in the host displaying stronger red luminescence than that from Eu^{3+}

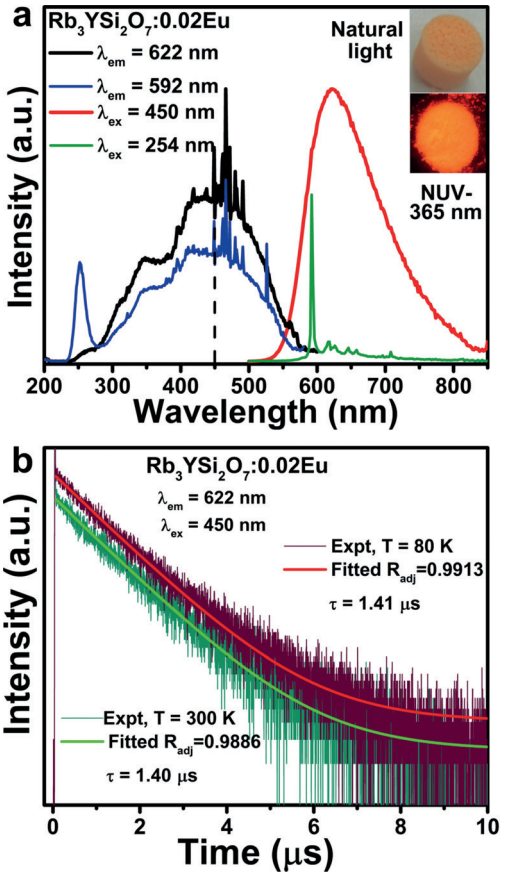

Figure 2. a) PLE and PL spectra of $Rb_3YSi_2O_7$:0.02Eu phosphors measured/monitored at room temperature (300 K) under different excitation (254, 450 nm) and emission (592, 622 nm) wavelengths, and the inset shows the as-prepared phosphor images under natural daylight and 365 nm UV light. b) Decay curves of the 622 nm emission from $Rb_3YSi_2O_7$:0.02Eu at room temperature (300 K) and low temperature (80 K), under excitation at 450 nm.

under blue-light excitation. This is because the 5d→4f emissive transitions of Eu^{2+} are spin- and parity-allowed, and its transition line strength is at least 10^4 times larger than those of the $(4f^6)^5D_0\rightarrow(4f^6)^7F_J$ transitions of Eu^{3+} which are spin- and parity-forbidden.[18]

The emission (excitation) spectra measured (monitored) under different excitation (emission) wavelengths are presented in the Supporting Information, Figure S3. The maximum of the emission spectrum (Supporting Information, Figure S3a) shows a slight red-shift with increasing excitation wavelength, which could be due to a change of relative contributions of Eu^{2+} and Eu^{3+} transitions to the emission spectrum with excitation wavelength. Besides, the onsets of the excitation spectra of the emissions at 700–740 nm display a slight red-shift with respect to those of the 550–620 nm emissions (Supporting Information, Figure S3b). This indicates the presence of another type of Eu^{2+} activators that account for the long-wavelength tail of the emission, with the coordination environments different from those responsible for the major portion of the emission spectrum.

To further investigate this point, the decay behaviors of the emissions at different wavelengths were measured. Figure 2b shows the decay behaviors of the 620 nm emission at

80 and 300 K can be well fitted by single exponential functions with the derived lifetimes of around 1.41 μs. This indicates that there is only one dominant type of Eu^{2+} activators in $Rb_3YSi_2O_7$, in agreement with the above spectral analysis. To certify the existence of another type of Eu^{2+} activators giving rise to the emission tail, the decay curves of the emissions at 700–760 nm were also monitored at 80 K (Supporting Information, Figure S4), and the fitting results are listed in the Supporting Information, Table S5. The decay curves of the 700, 720, and 740 nm emissions can be fitted by double-exponential functions with the fast and slow components of the decay time denoted by τ_1 and τ_2, respectively. With the increase of monitored emission wavelength, the values of τ_1 and τ_2 remain nearly constant at around 1.41 and 2.74 μs, with their contributions to the average decay time becoming relatively less and more important, respectively. For the emission at 760 nm, the decay curve becomes single exponential again with the fitted decay time of 2.75 μs. Therefore, the decay behaviors of the emissions at different wavelengths reflect also the presence of two different types of Eu^{2+} centers in $Rb_3YSi_2O_7$. One type is dominant with a shorter luminescence decay time than the other type which is the cause of the long-wavelength emission tail.

Eu^{2+} Site Occupations by DFT

A comparison of the ionic radii of Eu^{2+}, Rb^+, and Y^{3+} (Supporting Information, Table S4) would suggest that Eu^{2+} were located at Rb1 and/or Rb2 sites. To check this point, we have investigated Eu^{2+} site occupation in $Rb_3YSi_2O_7$ with DFT calculations. Two types of defect complexes, Eu_{Rb}-V_{Rb} and Eu_{Rb}-Eu_Y, were considered, and the corresponding substitution scenarios can be represented as:

$$Eu + Rb_3YSi_2O_7 = Rb_3YSi_2O_7{:}\ Eu_{Rb}\text{-}V_{Rb} + 2\,Rb$$

and

$$Eu + Rb_3YSi_2O_7 = Rb_3YSi_2O_7{:}\ Eu_{Rb}\text{-}Eu_Y + Rb + Y$$

The defect formation energies were calculated, respectively, by

$$E_f = E(\text{doped}) - E(\text{undoped}) + \mu_{Rb} + \mu_Y - \mu_{Eu}$$

and

$$E_f = E(\text{doped}) - E(\text{undoped}) + 2\mu_{Rb} - \mu_{Eu}$$

where E(doped) and E(undoped) denote the DFT total energies of the undoped and doped supercells. μ is the chemical potential of Rb, Y, or Eu and was approximated by the energy of the corresponding metallic atom in view of the reducing atmosphere used during the material synthesis.

All of the symmetrically different Eu_{Rb}-V_{Rb} and Eu_{Rb}-Eu_Y configurations within the $2\times2\times1$ supercell have been taken into account, including 15 Eu_{Rb1}-V_{Rb1}, 8 Eu_{Rb1}-V_{Rb2}, 16 Eu_{Rb2}-V_{Rb1}, 7 Eu_{Rb2}-V_{Rb2}, 16 Eu_{Rb1}-Eu_Y, and 8 Eu_{Rb2}-Eu_Y. The calculated defect formation energies per Eu^{2+} are listed in the Supporting Information, Table S6, where the negative E_f value indicates that the configuration is thermodynamically stable. To further quantify the relative preference of the substitutions, the occurrence probability for each defect complex was evaluated according to $P_i = \frac{1}{z_{tot}}\exp(-\frac{E_i}{kT})$, ($i$ = 1, …, 70), where z_{tot} is the partition function, E_i is the defect formation energy, k is the Boltzmann constant, and T (= 1423 K) is the synthesis temperature of the material. By summing the values of P_i for each kind of configurations (Figure 3), we found that the Eu^{2+} has a much higher tendency to be at the $Rb2^+$ site than at the $Rb1^+$ site (0.93 versus 0.07), with the excess charge compensated by V_{Rb} and Eu_Y substitutions in the order of decreasing probability. Moreover, Eu^{2+} has a non-negligible probability (0.091) of occupying the Y^{3+} site, acting as a charge compensator for Eu^{2+} substitution at the $Rb2^+$ site. Therefore, from a thermodynamic point of view, dopants Eu^{2+} are predicted to be mostly located at $Rb2^+$ sites with a small fraction at Y^{3+} sites.

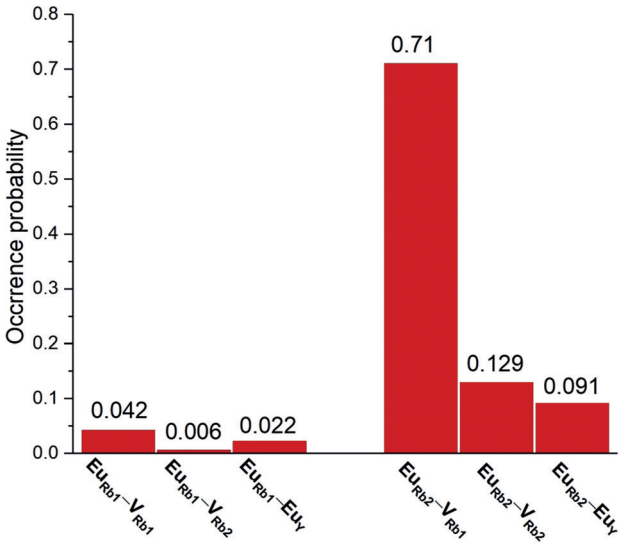

Figure 3. Calculated occurrence probabilities for different Eu_{Rb}-V_{Rb} and Eu_{Rb}-Eu_Y defect complexes in $Rb_3YSi_2O_7$.

Here, we discuss further the site origin of the red emission in $Rb_3YSi_2O_7$:0.02Eu. The 4f–5d transition energy of Eu^{2+} ions can be described as:[19]

$$E_{em}(A) = E_{free} - \varepsilon_c(A) - \frac{\varepsilon_{cfs}(A)}{r(A)} - \Delta S \quad (1)$$

where E_{free} is the 4f–5d transition energy of the free Eu^{2+} ion and $\varepsilon_c(A)$ and $\varepsilon_{cfs}(A)$ are the centroid shift and the crystal field splitting of the 5d orbitals, respectively. $r(A)$ represents the ratio of the crystal field contributing to the red-shift, and ΔS is the Stokes shift. For oxide phosphors, the factor $\varepsilon_c(A)$ has a small contribution to red-shift due to the weak covalence between Eu^{2+} and O^{2-} ions.[20] ΔS is related to distortion of polyhedra occupied by Eu^{2+} ions.[21] Usually, a higher distorted environment will induce a larger Stokes shift due to a significant reorganization of the coordinating atoms around Eu^{2+} in the 5d excited state.[22] In $Rb_3YSi_2O_7$, the distortion indices are 0, 0.0309, and 0 for the YO_6, $Rb1O_9$, and Rb_2O_6 polyhedra, respectively (Supporting Information, Table S7). The selective occupations of Eu^{2+} in the highly symmetrical polyhedra, $Rb2O_6$ and YO_6, are expected to result in a small ΔS, which is 3434 cm^{-1} in $Rb_3YSi_2O_7$. Thus, the red emission of $Rb_3YSi_2O_7$:Eu^{2+} can be ascribed mainly to the large crystal-field splitting, as a result of the small CNs and the small bond length. To further confirm this, the CNs and

average bond lengths of Rb-O and Y-O polyhedra in $Rb_3YSi_2O_7:Eu^{2+}$ are compared with other Rb and Y based phosphors (Supporting Information, Table S8). Obviously, the CNs and bond lengths of Rb-O polyhedra in $Rb_3YSi_2O_7:Eu^{2+}$ are smaller than those of $RbLi(Li_3SiO_4)_2:Eu^{2+}$, $RbNa_3(Li_3SiO_4)_4:Eu^{2+}$, and $RbBaSc Si_3O_9:Eu^{2+}$. The same trend is observed for Y-O polyhedra when compared with that of $Sr_3Y_2(Si_3O_9)_2:Eu^{2+}$ and $Ba_2Y_3(SiO_4)_3F:Eu^{2+}$ phosphors.[23] Thus, it is reasonable to conclude that small CNs and small bond lengths contribute to the unique red emission in $Rb_3YSi_2O_7:Eu^{2+}$ phosphors. Moreover, the much smaller polyhedral size of YO_6 than that of $Rb2O_6$ is consistent with the assignment of the long-wavelength emission tail to Eu^{2+} at Y^{3+} sites.

Temperature Quenching Property and Application for WLED

As one of key parameters to evaluate a new phosphor used for WLEDs, the temperature quenching properties of $Rb_3YSi_2O_7$:0.02Eu powders were investigated. The temperature-dependent PL spectra (Figure 4a) measured from room temperature to 500 K show that the emission intensity decreases slowly and the emission peak blue-shift slightly as the temperature increases. The blue-shift is due to the different sensitivity response to temperature for the Eu^{2+} ions at $Rb2^+$ and Y^{3+} sites. Figure 4b shows the temperature dependent integrated luminescence intensity of $Rb_3YSi_2O_7$:0.02Eu. At 423 K (150 °C), the integrated intensity remains about 80% of the initial intensity at 300 K (27 °C) with robustness towards thermal stability, which is better than that of commercial silicate phosphors, such as $Ba_2SiO_4:Eu^{2+}$ and $Sr_3SiO_5:Eu^{2+}$ (Supporting Information, Figure S5).[24] The excellent temperature-quenching behavior indicates that $Rb_3YSi_2O_7$:0.02Eu can be employed as a desirable phosphor for WLEDs. Under 445 nm excitation, the measured internal quantum efficiency of $Rb_3YSi_2O_7$:0.02Eu is about 32.6% (Supporting Information, Figure S6).

The CIE chromaticity coordinates for the $Rb_3YSi_2O_7$:Eu phosphor excited at 450 nm and the digital image upon the 365 nm UV lamp radiation are shown in Figure 4c. The CIE coordinates are calculated to be (0.653, 0.346) in the red region. To verify the potential application of $Rb_3YSi_2O_7$:0.02Eu red phosphor in solid-state lighting, the pc-WLEDs was fabricated by coating the mixture of $Rb_3YSi_2O_7$:Eu red and $Ba_2SiO_4:Eu^{2+}$ green phosphor on the 460 nm InGaN chip. Figure 4d shows the PL spectra, color-rendering index (Ra), color-correlated temperature (CCT), and luminous efficacy of as-fabricated WLED operated at 3.0 V with drive current 60 mA of the LED chip. The high color-rendering index ($R_a = 93$) and low color-correlated temperature (CCT = 4013 K) values indicate that $Rb_3YSi_2O_7$:Eu has potential to act as red-emitting phosphor for high quality WLEDs lighting. The PL spectra were also measured under different forward bias currents (60–160 mA; Figure 4e), and the detailed optical parameters for the wLED are shown in the Supporting Information, Table S9. The color coordinates of $Rb_3YSi_2O_7$:Eu based LED almost unchanged (Figure 4f) even at the high flux current of 160 mA. However, the measured luminous efficacy of as-fabricated wLED is only 33.96 lm W^{-1}, which may be improved in the future by synthesis optimization techniques and chemical substitution.

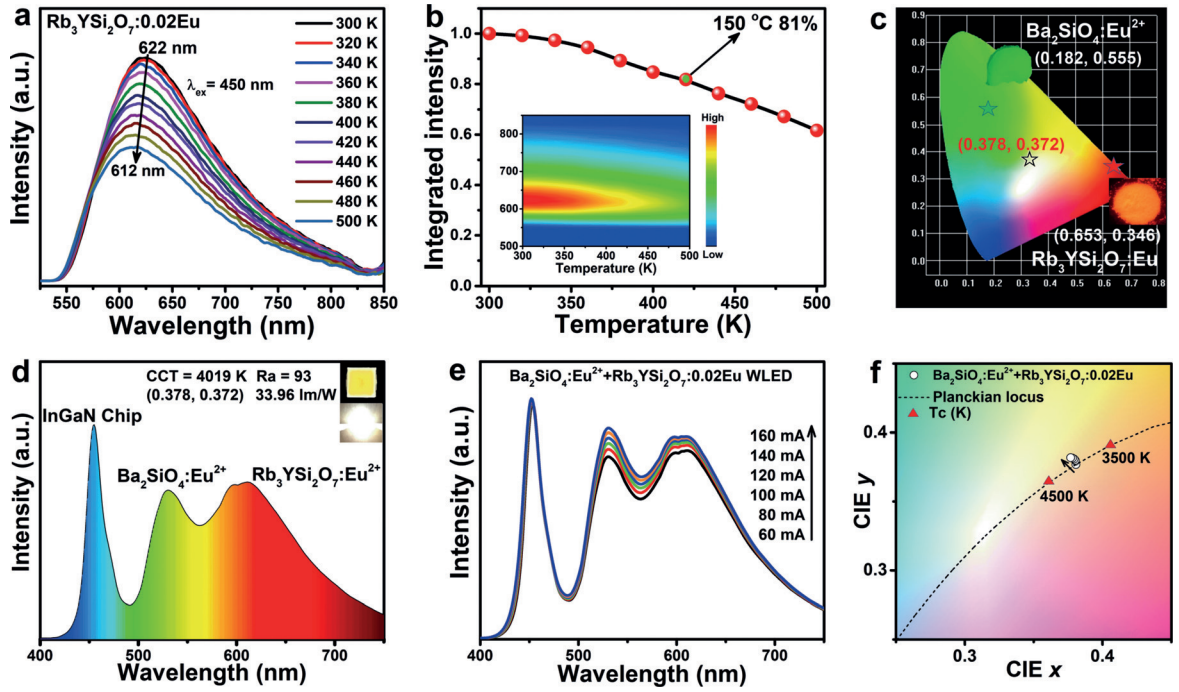

Figure 4. a) Temperature-dependent spectra of $Rb_3YSi_2O_7$:0.02Eu measured from 300 K to 500 K. b) Temperature-dependent normalized emission spectra of $Rb_3YSi_2O_7$:0.02Eu. c) CIE chromaticity diagram of the $Rb_3YSi_2O_7$:0.02Eu red phosphor, $Ba_2SiO_4:Eu^{2+}$ green phosphor and the fabricated WLEDs. d) PL spectrum and photograph of WLED devices fabricated with the commercial green phosphor $Ba_2SiO_4:Eu^{2+}$ and red phosphor $Rb_3YSi_2O_7$:0.02Eu on a blue LED chip (460 nm) under a current of 40 mA. e) EL spectra and f) CIE chromaticity coordinates of the fabricated WLED under various forward bias currents.

Conclusion

In summary, following the weak covalent interaction between Eu^{2+} and O^{2-}, red emission from Eu^{2+} in oxide phosphors can hardly be found, and thus the selective occupation of the inorganic polyhedra with small CNs can come into play. As found here that Eu^{2+} are located at $Rb2^{+}$ and Y^{3+} cation sites of $Rb_3YSi_2O_7$ both with CN = 6, a new oxide-based phosphor, $Rb_3YSi_2O_7$:Eu has been discovered demonstrating a broad-band red emission under 450 nm blue-light excitation. Relatively weak sharp line red emission was also observed and ascribed to Eu^{3+} located at Y^{3+} sites. The fabricated WLEDs based on $Rb_3YSi_2O_7$:0.02Eu and Ba_2SiO_4:Eu^{2+} phosphors showed high CRI ($R_a = 93$) and low CCT (4013 K), indicating that $Rb_3YSi_2O_7$:Eu can be used as an ideal red phosphor for high-quality pc-WLEDs. This finding on the screening of the site selective occupation toward the design of red phosphors can initiate more research to explore the synergetic effect on tailoring the emission color of Eu^{2+}-doped inorganic solid-state materials for WLEDs.

Acknowledgements

This work is supported by the National Natural Science Foundation of China (51722202, 51572023, and 11574003), Natural Science Foundations of Beijing (2172036), Fundamental Research Funds for the Central Universities (FRF-TP-18-002C1), and the Guangdong Provincial Science & Technology Project (2018A050506004). K.R.P. recognizes that this work was made possible by support from the National Science Foundation, Solid State Materials Chemistry award DMR-1608218.

Conflict of interest

The authors declare no conflict of interest.

Leuchtdioden · Positionsbesetzung · Rot emittierende Leuchtstoffe · Silicate

Zitierweise: *Angew. Chem. Int. Ed.* **2019**, *58*, –
Angew. Chem. **2019**, *131*, –

[1] a) H. S. Jang, Y. H. Won, D. Y. Jeon, *Appl. Phys. B* **2009**, *95*, 715 – 720; b) V. Bachmann, C. Ronda, A. Meijerink, *Chem. Mater.* **2009**, *21*, 2077 – 2084.
[2] a) P. Pust, P. J. Schmidt, W. Schnick, *Nat. Mater.* **2015**, *14*, 454 – 458; b) Z. Wang, J. Ha, Y. H. Kim, W. B. Im, J. McKittrick, S. P. Ong, *Joule* **2018**, *2*, 914 – 926.
[3] P. Pust, V. Weiler, C. Hecht, A. Tucks, A. S. Wochnik, A. K. Henss, D. Wiechert, C. Scheu, P. J. Schmidt, W. Schnick, *Nat. Mater.* **2014**, *13*, 891 – 896.
[4] C. Guo, D. Huang, Q. Su, *Mater. Sci. Eng. B* **2006**, *130*, 189 – 193.
[5] a) K. Uheda, N. Hirosaki, Y. Yamamoto, A. Naito, T. Nakajima, H. Yamamoto, *Electrochem. Solid-State Lett.* **2006**, *9*, H22 – H25; b) R.-J. Xie, N. Hirosaki, T. Suehiro, F.-F. Xu, M. Mitomo, *Chem. Mater.* **2006**, *18*, 5578 – 5583; c) L. Wang, R.-J. Xie, Y. Li, X. Wang, C.-G. Ma, D. Luo, T. Takeda, Y.-T. Tsai, R.-S. Liu, N. Hirosaki, *Light: Sci. Appl.* **2016**, *5*, e16155; d) L. Chen, M. Fei, Z. Zhang, Y. Jiang, S. Chen, Y. Dong, Z. Sun, Z. Zhao, Y. Fu, J. He, C. Li, Z. Jiang, *Chem. Mater.* **2016**, *28*, 5505 – 5515; e) J. Häusler, L. Neudert, M. Mallmann, R. Niklaus, A. C. L. Kimmel, N. S. Alt, E. Schlücker, O. Oeckler, W. Schnick, *Chem. Eur. J.* **2017**, *23*, 2583 – 2590.
[6] a) A. A. Setlur, E. V. Radkov, C. S. Henderson, J.-H. Her, A. M. Srivastava, N. Karkada, M. S. Kishore, N. P. Kumar, D. Aesram, A. Deshpande, B. Kolodin, L. S. Grigorov, U. Happek, *Chem. Mater.* **2010**, *22*, 4076 – 4082; b) T. Takahashi, S. Adachi, *J. Electrochem. Soc.* **2008**, *155*, E183 – E188.
[7] H. Zhu, C. C. Lin, W. Luo, S. Shu, Z. Liu, Y. Liu, J. Kong, E. Ma, Y. Cao, R. S. Liu, X. Chen, *Nat. Commun.* **2014**, *5*, 4312.
[8] a) Y. Sato, H. Kato, M. Kobayashi, T. Masaki, D. H. Yoon, M. Kakihana, *Angew. Chem. Int. Ed.* **2014**, *53*, 7756 – 7759; *Angew. Chem.* **2014**, *126*, 7890 – 7893; b) P. Zhang, L. Li, M. Xu, L. Liu, *J. Alloys Compd.* **2008**, *456*, 216 – 219; c) T. Zhou, Z. Song, X. Song, L. Bian, Q. Liu, *Chin. Phys. B* **2010**, *19*, 127808.
[9] P. Dorenbos, *J. Lumin.* **2003**, *104*, 239 – 260.
[10] H. Daicho, Y. Shinomiya, K. Enomoto, A. Nakano, H. Sawa, S. Matsuishi, H. Hosono, *Chem. Commun.* **2018**, *54*, 884 – 887.
[11] F. J. DiSalvo, S. J. Clarke, *Curr. Opin. Solid State Mater. Sci.* **1996**, *1*, 241 – 249.
[12] a) P. Dorenbos, *ECS J. Solid State Sci. Technol.* **2013**, *2*, R3001 – R3011; b) S. Wang, Z. Song, Y. Kong, Z. Xia, Q. Liu, *J. Lumin.* **2018**, *194*, 461 – 466.
[13] TOPAS V.2: General profile and structure analysis software for powder diffraction data-User's Manual; Bruker AXS: Karlsruhe, Germany, **2008**.
[14] A. M. Latshaw, G. Morrison, K. D. zur Loye, A. R. Myers, M. D. Smith, H.-C. zur Loye, *CrystEngComm* **2016**, *18*, 2294 – 2302.
[15] J.-F. Bérar, P. Lelann, *J. Appl. Crystallogr.* **1991**, *24*, 1 – 5.
[16] R. D. Shannon, *Acta Crystallogr. Sect. A* **1976**, *32*, 751 – 767.
[17] M. Zhao, Z. Xia, X. Huang, L. Ning, R. Gautier, M. S. Molokeev, Y. Zhou, Y.-C. Chuang, Q. Zhang, Q. Liu, *Sci. Adv.* **2019**, *5*, eaav0363.
[18] B. Henderson, G. F. Imbusch, *Optical spectroscopy of inorganic solids*, *Vol. 44*, Oxford University Press, **2006**.
[19] P. Dorenbos, *J. Lumin.* **2002**, *99*, 283 – 299.
[20] P. Dorenbos, *J. Phys. Condens. Matter* **2003**, *15*, 4797.
[21] A. Diaz, D. A. Keszler, *Mater. Res. Bull.* **1996**, *31*, 147 – 151.
[22] M. A. Lim, J. K. Park, C. H. Kim, H. D. Park, M. W. Han, *J. Mater. Sci. Lett.* **2003**, *22*, 1351 – 1353.
[23] a) M. Zhao, H. Liao, L. Ning, Q. Zhang, Q. Liu, Z. Xia, *Adv. Mater.* **2018**, *30*, 1802489; b) S. Ray, P. Tadge, S. J. Dhoble, G. B. Nair, A. Singh, A. K. Singh, M. Rai, T. M. Chen, V. Rajput, *J. Alloys Compd.* **2017**, *713*, 138 – 147; c) M. Zhang, Y. Liang, S. Xu, Y. Zhu, X. Wu, S. Liu, *CrystEngComm* **2016**, *18*, 68 – 76; d) J. Wang, H. Lin, Q. Huang, G. Xiao, J. Xu, B. Wang, T. Hu, Y. Wang, *J. Mater. Chem. C* **2017**, *5*, 1789 – 1797; e) H. Liao, M. Zhao, M. S. Molokeev, Q. Liu, Z. Xia, *Angew. Chem. Int. Ed.* **2018**, *57*, 11728 – 11731; *Angew. Chem.* **2018**, *130*, 11902 – 11905.
[24] a) Z. Ci, M. Que, Y. Shi, G. Zhu, Y. Wang, *Inorg. Chem.* **2014**, *53*, 2195 – 2199; b) L. He, Z. Song, X. Jia, Z. Xia, Q. Liu, *Inorg. Chem.* **2018**, *57*, 609 – 616.
[25] CCDC 1909273 contains the supplementary crystallographic data for this paper. These data can be obtained free of charge from The Cambridge Crystallographic Data Centre.

Manuskript erhalten: 9. Mai 2019
Veränderte Fassung erhalten: 25. Mai 2019
Akzeptierte Fassung online: 5. Juni 2019
Endgültige Fassung online: 2. Juli 2019

